Nonlinear Unmixing of Hyperspectral Data Using Semi-Nonnegative Matrix Factorization

Naoto Yokoya, *Student Member*, IEEE, Jocelyn Chanussot, *Fellow, IEEE*, and Akira Iwasaki

Abstract—**Nonlinear spectral mixture models have recently received particular attention in hyperspectral image processing. In this paper, we present a novel optimization method of nonlinear unmixing based on a generalized bilinear model (GBM), which considers the second–order scattering of photons in a spectral mixture model. Semi-nonnegative matrix factorization (semi-NMF) is used for the optimization to process a whole image in matrix form. When endmember spectra are given, the optimization of abundance and interaction abundance fractions converge to a local optimum by alternating update rules with simple implementation. The proposed method is evaluated using synthetic datasets considering its robustness for the accuracy of endmember extraction and spectral complexity, and shows smaller errors in abundance fractions rather than conventional methods. GBM-based unmixing using semi-NMF is applied to the analysis of an airborne hyperspectral image taken over an agricultural field with many endmembers, and it visualizes the impact of a nonlinear interaction on abundance maps at reasonable computational cost.**

Index Terms—**Generalized bilinear model (GBM), nonlinear unmixing, semi-nonnegative matrix factorization.**

I. INTRODUCTION

SPECTRAL unmixing is an important task for hyperspectral image interpretation. Many researchers have worked on this problem using a linear mixture model (LMM), in which it is assumed that an observed spectrum is a linear combination of several endmember spectra. The LMM is a simplified spectral mixture model that considers only first-order scattered photons by neglecting multiple photon interactions. Although LMM-based unmixing methods can retrieve physically meaningful results, nonlinearity in a spectral mixture model has been pointed out in many works [1]–[12]. In recent years, nonlinear unmixing for hyperspectral images has been receiving particular attention in remote sensing image exploitation. Nonlinear spectral mixing occurs owing to multiple reflections and transmissions from a surface [2]. Bioucas–Dias *et al.* [13] classified nonlinear unmixing into two scenarios: an intimate

mixture and a multilayered scene. The intimate mixture model is based on the photometric model of Hapke [14], which considers multiple scattering between different materials at the particle level [6]. Close *et al.* [7], [8] applied Hapke's average albedo model to solve fully unsupervised nonlinear unmixing in the case of intimate mixtures. In the multilayered scene, there are multiple interactions among scatters at different layers, which often happen between vegetation and soil [1]–[5]. The bilinear mixture model (BMM) considers the second-order scattering of photons between two distinct materials and introduces additional virtual endmembers formed by their product terms into the LMM [3]. The BMM is a common model of nonlinear unmixing in multilayered scenes, and its optimization has been studied with different constraints by several groups [5], [9]–[11]. Chen *et al.* [16] analyzed the impact of the collinearity effect [15] of virtual endmembers on bilinear spectral unmixing. When there is a high correlation between endmembers and second-order scattering virtual endmembers and when hyperspectral data contain severe noise, the optimization based on [5] resulted in worse abundance estimation than linear spectral mixture analysis. Halimi *et al.* [11] introduced the generalized bilinear model (GBM) as an effective means of dealing with the underlying assumptions in the BMM. The GBM method was applied to the analysis of small images of synthetic and real hyperspectral data with three endmembers and showed good results [11], [12]. When applied to the analysis of larger images in an unsupervised manner with more endmembers, the optimization becomes more challenging owing to the collinearity and the various possibilities of local minima.

Nonnegative matrix factorization (NMF) [17], [18], which factorizes a nonnegative matrix into two nonnegative matrices, has recently emerged as a useful method of solving the LMM-based unmixing problem [19]–[22]. Ding *et al.* [23] proposed a new variation in the theme of NMF, i.e., a semi-nonnegative matrix factorization (semi-NMF) that factorizes a nonrestricted matrix into a nonrestricted matrix and a nonnegative matrix. In this paper, we present semi-NMF as a novel optimization method for GBM-based unmixing. We evaluate it using synthetic datasets and apply it to the analysis of a real hyperspectral image with 10 endmembers. We also investigate the effect of endmember extraction on nonlinear unmixing and visualize the impact of second-order scattering effects on abundance maps.

The rest of this paper is organized as follows. In Section II, we describe semi-NMF for GBM-based unmixing. In Section III, we evaluate the proposed method using

N. Yokoya and A. Iwasaki are with the Department of Aeronautics and Astronautics, University of Tokyo, Tokyo 153-0041, Japan (e-mail: yokoya@sal.rcast.u-tokyo.ac.jp; aiwasaki@sal.rcast.u-tokyo.ac.jp).

J. Chanussot is with the Grenoble Institute of Technology, Saint Martin d'Hères cedex 38402, France (e-mail: jocelyn.chanussot@gipsa-lab.grenoble-inp.fr).

synthetic datasets, comparing it with conventional methods. We present the experimental results for real data in Section IV, and conclude this paper in Section V.

II. GBM-BASED UNMIXING VIA SEMI-NONNEGATIVE MATRIX FACTORIZATION

A. Generalized Bilinear Model

The BMM takes account of second-order photon interactions between different D endmembers as additional terms in the LMM, assuming that third or higher order interactions are negligible [5]. In the BMM, the observed L spectrum of a single pixel $\mathbf{y} \in \mathbb{R}^{L \times 1}$ is given by

$$\mathbf{y} = \mathbf{Ea} + \sum_{(i,j) \in G} b_{i,j} \mathbf{e}_i \odot \mathbf{e}_j + \mathbf{n}$$

$$G = \{(i,j) | i < j, i \in \{1, \ldots, D\}, j \in \{1, \ldots, D\}\} \quad (1)$$

where $\mathbf{E} \in \mathbb{R}^{L \times D}$ is the endmember matrix with the ith column vector $\{\mathbf{e}_i\}_{i=1}^{D} \in \mathbb{R}^{L \times 1}$ representing the ith endmember spectrum, $\mathbf{a} \in \mathbb{R}^{D \times 1}$ is the abundance vector, $b_{i,j}$ is the interaction abundance between the ith and jth endmembers, $\odot$ is the Hadamard (element-wise product) operation, and $\mathbf{n} \in \mathbb{R}^{L \times 1}$ is the additive noise. On the right-hand side, the first term denotes linear mixing, and the second term represents a second-order interaction, which is assumed to be a linear combination of the cross-products of the interacting virtual endmembers, i.e., the bilinear spectral mixing. The constraint $i < j$ defined in (1) is based on the commutative property of the Hadamard operation, i.e., $\mathbf{e}_i \odot \mathbf{e}_j = \mathbf{e}_j \odot \mathbf{e}_i$. On the assumption that an endmember spectrum is a representative of the multi-order self-interaction, the ith pure endmember spectrum $\mathbf{e}_i = (e_{i1}, \ldots, e_{iL})^T \in \mathbb{R}^{L \times 1}$ is defined by a power series of the self-interaction

$$e_{ik} = \sum_{n=1}^{\infty} \alpha_n f_{ik}^n \quad (2)$$

where e_{ik} ($k \in \{1, \ldots, L\}$) is the kth element of the endmember spectrum $\mathbf{e}_i$, α_n is the abundance of nth-order self-interaction, and $\mathbf{f}_i = (f_{i1}, \ldots, f_{iL})^T \in \mathbb{R}^{L \times 1}$ is the first-order self-interaction spectrum of the ith endmember. Consequently, $b_{i,i}$ corresponding to the second-order self-interaction is eliminated in (1) because the second-order self-interaction term, i.e., $n = 2$, is inherent in the endmember matrix $\mathbf{E}$.

From a physical perspective, the GBM introduces the nonlinear mixing coefficient $b_{i,j}$ as $b_{i,j} = c_{i,j} a_i a_j$ and assumes the following constraints:

$$a_i \geq 0 \quad i \in \{1, \ldots, D\} \quad \text{and} \quad \sum_{i=1}^{D} a_i = 1 \quad (3)$$

$$0 \leq c_{i,j} \leq 1$$
$$i < j$$
$$i \in \{1, \ldots, D\}, \quad j \in \{1, \ldots, D\}. \quad (4)$$

When the endmember spectra are known, GBM-based unmixing turns to the optimization of the abundance ($\mathbf{a}$) and the interaction coefficient ($\mathbf{c}$) under the constraints of (3) and (4).

Halimi *et al.* [12] proposed three optimization methods using different algorithms: the Bayesian algorithm using the Markov-chain Monte Carlo method; the Fan-FCLS algorithm; and the gradient descent algorithm (GDA). The GDA showed good results for both synthetic and real hyperspectral datasets.

B. Semi-Nonnegative Matrix Factorization for GBM

In this paper, the new optimization method based on semi-NMF is introduced to speed up the optimization of a whole image in matrix form. The observed hyperspectral image can be reshaped as a matrix form $\mathbf{Y} \in \mathbb{R}^{L \times P}$, with P representing the number of pixels. The BMM for the whole image is given in matrix form by

$$\mathbf{Y} = \mathbf{EA} + \mathbf{MB} + \mathbf{N} \quad (5)$$

where $\mathbf{A} \in \mathbb{R}^{D \times P}$ is the abundance matrix with each column vector $\{\mathbf{a}_l\}_{l=1}^{P} \in \mathbb{R}^{D \times 1}$ representing the abundance vector at the lth pixel, $\mathbf{M} \in \mathbb{R}^{L \times D(D-1)/2}$ is the bilinear endmember matrix, $\mathbf{B} \in \mathbb{R}^{D(D-1)/2 \times P}$ is the interaction abundance matrix with each column vector $\{\mathbf{b}_l\}_{l=1}^{P} \in \mathbb{R}^{D(D-1)/2 \times 1}$ representing the interaction abundance vector at the lth pixel, and $\mathbf{N} \in \mathbb{R}^{L \times P}$ is the noise matrix. GBM-based unmixing becomes the following minimization with respect to $\mathbf{A}$ and $\mathbf{B}$:

$$\text{minimize} \ \|\mathbf{Y} - \mathbf{EA} - \mathbf{MB}\|_F^2 \quad (6)$$

$$\text{subject to } \mathbf{A} \succeq \mathbf{0}, \quad \sum_{i=1}^{D} (\mathbf{A})_{il} = 1, \quad \mathbf{0} \preceq \mathbf{B} \preceq \mathbf{A}^* \ (7)$$

where $(\mathbf{A}^*)_{(i,j)l} = (\mathbf{A})_{il}(\mathbf{A})_{jl}$ ($l \in \{1, \ldots, P\}$), the operator $\|\cdot\|_F$ denotes the Frobenius norm, and the symbol $\preceq$ denotes inequality component-wise. By introducing $\mathbf{Y}_1 = \mathbf{Y} - \mathbf{MB}$ and $\mathbf{Y}_2 = \mathbf{Y} - \mathbf{EA}$, (5) is written as

$$\mathbf{Y}_1 = \mathbf{EA} + \mathbf{N} \quad (8)$$
$$\mathbf{Y}_2 = \mathbf{MB} + \mathbf{N}. \quad (9)$$

Alternately minimizing $\|\mathbf{Y}_1 - \mathbf{EA}\|_F^2$ and $\|\mathbf{Y}_2 - \mathbf{MB}\|_F^2$ with respect to $\mathbf{A}$ and $\mathbf{B}$, respectively, can be used for the local optimization of the original problem (6) performed using an alternating optimization algorithm. Owing to physical constraints, all the components of $\mathbf{E}$, $\mathbf{M}$, $\mathbf{A}$, and $\mathbf{B}$ are nonnegative. Therefore, the minimization of (6) can be done using alternative update rules of semi-NMF [23]. Semi-NMF is a problem that factorizes the nonrestricted matrix $\mathbf{X}$ into the nonrestricted matrix $\mathbf{F}$ and the nonnegative matrix $\mathbf{G}$ such that $\mathbf{X} = \mathbf{FG}^T$ [23]. Ding *et al.* [23] proposed an iterative updating algorithm that alternatively updates $\mathbf{F}$ and $\mathbf{G}$ using

$$\mathbf{F} = \mathbf{XG}(\mathbf{G}^T\mathbf{G})^{-1} \quad (10)$$

$$\mathbf{G} \leftarrow \mathbf{G}.*\sqrt{\left((\mathbf{X}^T\mathbf{F})^+ + \mathbf{G}(\mathbf{F}^T\mathbf{F})^-\right)./\left((\mathbf{X}^T\mathbf{F})^- + \mathbf{G}(\mathbf{F}^T\mathbf{F})^+\right)} \quad (11)$$

where $.*$ and $./$ denote multiplication and division element-wise. $(\mathbf{C})^+$ and $(\mathbf{C})^-$ are the positive and negative parts of the matrix $\mathbf{C}$ defined as $\mathbf{C}^+ = (|\mathbf{C}| + \mathbf{C})/2$, $\mathbf{C}^- = (|\mathbf{C}| - \mathbf{C})/2$. Semi-NMF optimization is guaranteed to converge to a local optimum using alternative updating rules.

When $\mathbf{E}$ is given and $\mathbf{M}$ is calculated from $\mathbf{E}$, GBM-based unmixing is solved using the following update rules for $\mathbf{A}$ and $\mathbf{B}$:

$$\mathbf{A}^T \leftarrow \mathbf{A}^T .* \sqrt{\left(\left(\mathbf{Y}_1^T \mathbf{E}\right)^+ + \mathbf{A}^T \left(\mathbf{E}^T \mathbf{E}\right)^-\right)./\left(\left(\mathbf{Y}_1^T \mathbf{E}\right)^- + \mathbf{A}^T \left(\mathbf{E}^T \mathbf{E}\right)^+\right)} \tag{12}$$

$$\mathbf{B}^T \leftarrow \mathbf{B}^T .* \sqrt{\left(\left(\mathbf{Y}_2^T \mathbf{M}\right)^+ + \mathbf{B}^T \left(\mathbf{M}^T \mathbf{M}\right)^-\right)./\left(\left(\mathbf{Y}_2^T \mathbf{M}\right)^- + \mathbf{B}^T \left(\mathbf{M}^T \mathbf{M}\right)^+\right)}. \tag{13}$$

Since semi-NMF converges to a local optimum, initialization is critical to the final results. We assume that the LMM can be an approximation of the BMM. The fully constrained least-squares (FCLS) method [24], which is a well-known abundance estimation method based on the LMM, is used to initialize the abundance matrix $\mathbf{A}$, and the interaction abundance matrix $\mathbf{B}$ is initialized as $\delta \times \mathbf{A}^*$ with a small δ.

For any observed spectrum ($\mathbf{y}$), the linear mixing term is larger than the bilinear mixing term

$$\mathbf{Ea} - \mathbf{Mb} \succeq \sum_{i=1}^D a_i \mathbf{e}_i - \sum_{(i,j) \in G} a_i a_j \mathbf{e}_i \odot \mathbf{e}_j$$
$$\succeq \sum_{i=1}^D a_i \mathbf{e}_i \left(1 - \frac{\sum_{j \neq i} a_j}{2}\right)$$
$$= \sum_{i=1}^D a_i \mathbf{e}_i \left(\frac{1 + a_i}{2}\right) \succeq \mathbf{0}. \tag{14}$$

When the signal-to-noise ratio (SNR) between $\mathbf{Ea} + \mathbf{Mb}$ and $\mathbf{n}$ is larger than 2, the SNR between $\mathbf{Ea}$ and $\mathbf{n}$ is larger than 1. Generally, the SNR of hyperspectral sensors is much larger than 2; therefore, all components of $\mathbf{Y}_1$ can be assumed to be nonnegative. In this case, the minimizing the cost function $\|\mathbf{Y}_1 - \mathbf{EA}\|_F^2$ can be done by NMF [17], which factorizes a nonnegative matrix into two nonnegative matrices. $\mathbf{A}$ can converge to a local optimum by the NMF update rule given by

$$\mathbf{A} \leftarrow \mathbf{A} .* \left(\mathbf{E}^T \mathbf{Y}_1\right) ./ \left(\mathbf{E}^T \mathbf{EA}\right). \tag{15}$$

If any component of $\mathbf{Y}_1$ is negative owing to extreme noise at the beginning, it should be initialized to zero.

The convergence property based on the update rules of (12) and (13) or (15) and (13) is proved as follows. In [23], it is guaranteed that, by fixing $\mathbf{E}$, the residual error $\|\mathbf{Y}_1 - \mathbf{EA}\|_F^2$ ($\|\mathbf{Y} - \mathbf{EA} - \mathbf{MB}\|_F^2$) decreases monotonically under the update rule for $\mathbf{A}$. In the same way, by fixing $\mathbf{M}$, the residual error $\|\mathbf{Y}_2 - \mathbf{MB}\|_F^2$ ($\|\mathbf{Y} - \mathbf{EA} - \mathbf{MB}\|_F^2$) decreases monotonically under the update rule for $\mathbf{B}$. Therefore, $\|\mathbf{Y} - \mathbf{EA} - \mathbf{MB}\|_F^2$ decreases monotonically under the update rules (12) and (13). In [18], it is also proved that, when $\mathbf{Y}_1$ is nonnegative, $\|\mathbf{Y}_1 - \mathbf{EA}\|_F^2$ ($\|\mathbf{Y} - \mathbf{EA} - \mathbf{MB}\|_F^2$) decreases under the update rule (15). Therefore, $\|\mathbf{Y} - \mathbf{EA} - \mathbf{MB}\|_F^2$ decreases monotonically with the alternative updating of (15) and (13). The algorithm of GBM-based unmixing using semi-NMF is as follows.

Algorithm 1 Generalized Bilinear Model-Based Nonlinear Unmixing Via Semi-NMF

Input: Hyperspectral data $\mathbf{Y} \in \mathbb{R}^{L \times P}$ and endmember matrix $\mathbf{E} \in \mathbb{R}^{L \times D}$.

Output: Abundance matrix $\mathbf{A} \in \mathbb{R}^{D \times P}$ and interaction abundance matrix $\mathbf{B} \in \mathbb{R}^{D(D-1)/2 \times P}$.

Step 1: $\mathbf{A}$ is initialized using FCLS based on the LMM.

Step 2: $\mathbf{A}^*$ is calculated and $\mathbf{B}$ is set as $\delta \times \mathbf{A}^*$ with a small δ.

Step 3: $\mathbf{A}$ and $\mathbf{B}$ are alternatively updated using (12) and (13) (semi-NMF only) or (15) and (13) (NMF and semi-NMF). If any element of $\mathbf{B}$ exceeds that of $\mathbf{A}^*$, it is replaced with that of $\mathbf{A}^*$.

To satisfy the abundance sum-to-1constraint, the method cited from [24] is adopted.

III. EVALUATION OF SYNTHETIC DATA

Synthetic hyperspectral images (20×20 pixel size) are used to evaluate the unmixing performance of the proposed method, considering the robustness of the algorithm for the accuracy of endmember spectra and the collinearity issue. Since bilinear spectral mixing often occurs between vegetation and soil [1]–[5], four spectra, i.e., the spectra of two types of plants, soil, and water in the U. S. Geological Survey spectral library, are selected as materials of synthetic images. The leaves of spurge and oak are chosen as vegetation, and the Stonewall Playa surface is used as soil. The original endmember spectra are spectrally downsampled with the spectral characteristic of the Airborne Visible/Infrared Imaging Spectrometer. To evaluate the robustness of the algorithm for spectral complexity and the collinearity issue, two types of synthetic dataset with different combinations of endmembers are generated using three (spurge leaf, soil, and water) and four endmember spectra, respectively. For each combination of endmembers, we use three different spectral mixing models, i.e., the LMM (image 1), the GBM (image 2), and a hybrid of the LMM and GBM (image 3). The half pixels in the hybrid image are generated by the LMM and GBM. To obtain synthetic images without pure pixels, all abundance fractions are generated uniformly on a simplex with a cutoff threshold fixed at 0.8. For the GBM, the interaction coefficients are set using uniformly distributed random values in [0 1]. Gaussian noises are added to all images, setting SNR to 20, which is generally a noise condition worse than that for real hyperspectral data. Two scenarios are used for endmember extraction. In the first scenario, true endmember spectra are given. In the second scenario, vertex component analysis (VCA) [25], which is one of the most common convex-geometry-based endmember extraction methods that entail a pure-pixel assumption, is used for endmember extraction.

First, we compare the performances of the proposed two methods, i.e., the semi-NMF-only optimization and the NMF and semi-NMF optimization, using synthetic datasets generated using three endmembers. We adopt two criteria, i.e., the reconstruction error (RE) of unmixing, and the root mean
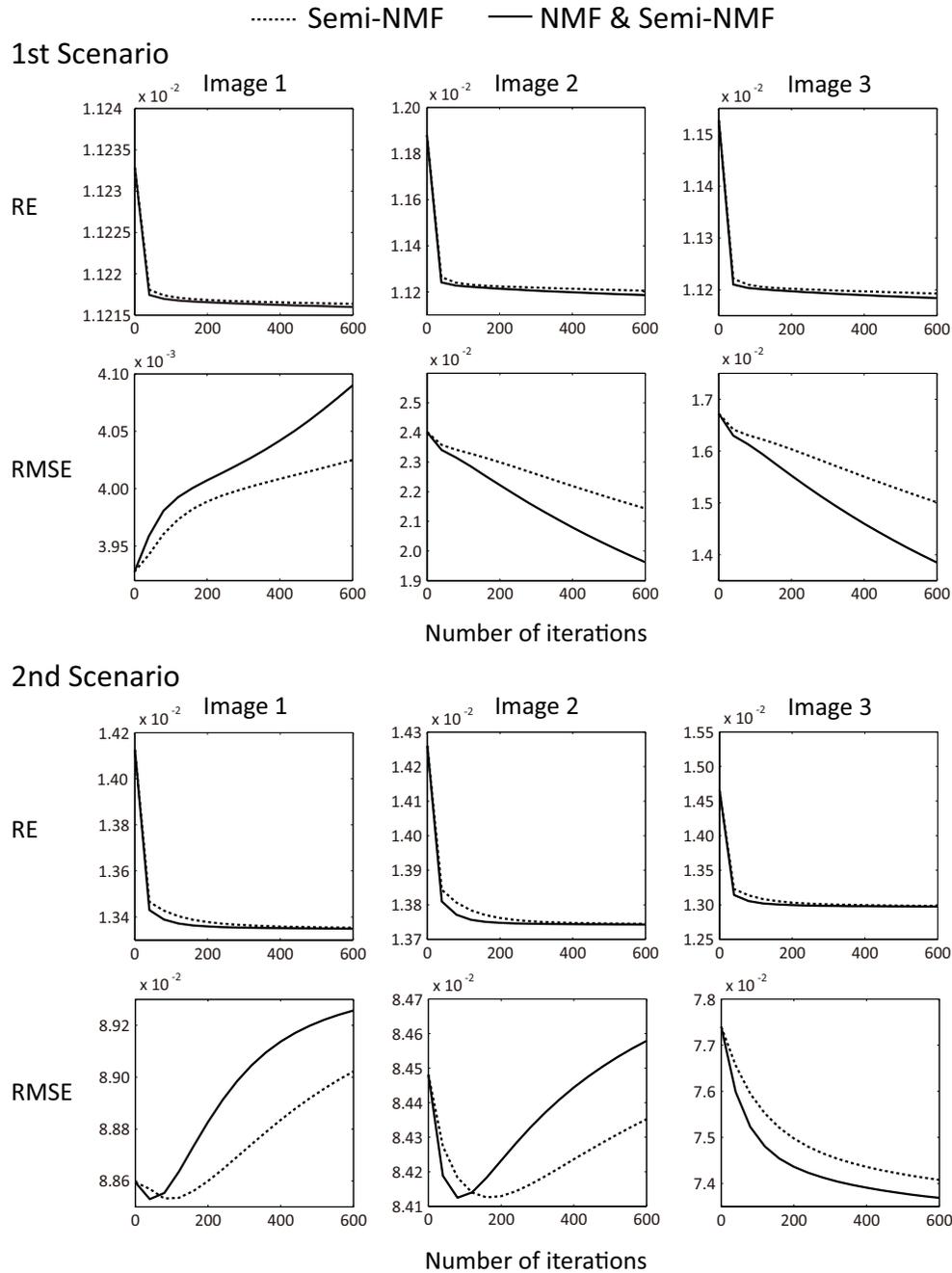
Fig. 1.   Changes in RE of unmixing and RMSE of abundance with number of iterations.

square error (RMSE) of abundance fractions. The RE of unmixing is calculated to measure the distance between the observed ($\mathbf{y}_l$) and estimated ($\widehat{\mathbf{y}}_l$) spectra as

$$\mathrm{RE} = \sqrt{\frac{1}{LP} \sum_{l=1}^{P} \|\widehat{\mathbf{y}}_l - \mathbf{y}_l\|^2}. \tag{16}$$

The RMSE of abundance fractions is the most important criterion for evaluating unmixing performance, which can be used to compute the accuracy of estimated abundance maps using the actual ($\mathbf{a}_i$) and estimated ($\widehat{\mathbf{a}}_i$) abundances as

$$\mathrm{RMSE} = \sqrt{\frac{1}{DP} \sum_{i=1}^{D} \|\widehat{\mathbf{a}}_i - \mathbf{a}_i\|^2}. \tag{17}$$

Fig. 1 shows the changes in the RE of unmixing and in the RMSE of abundance fractions with the number of iterations for three synthetic images. In the first scenario, the NMF and semi-NMF optimizations show faster convergence for images 2 and 3 in the RE of unmixing and smaller RMSEs of abundance fractions, which monotonically decrease. In the case of image 1, which is based on the LMM, the RMSE of abundance fractions increases in both methods because the FCLS method converges to a global optimum. In the second scenario, the NMF and semi-NMF optimizations show faster convergence in the RE of unmixing for all the datasets; however, the RMSE of abundance fractions increases after convergence for image 2. This means that overfitting occurs in the optimization when the estimated endmember spectra
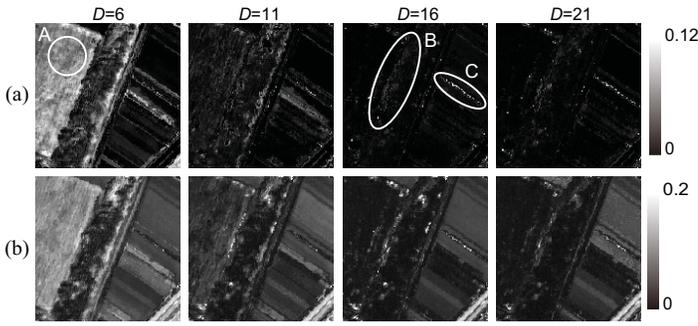
Fig. 2.   (a) RSS maps of second-order interaction terms. (b) Unmixing residual errors.
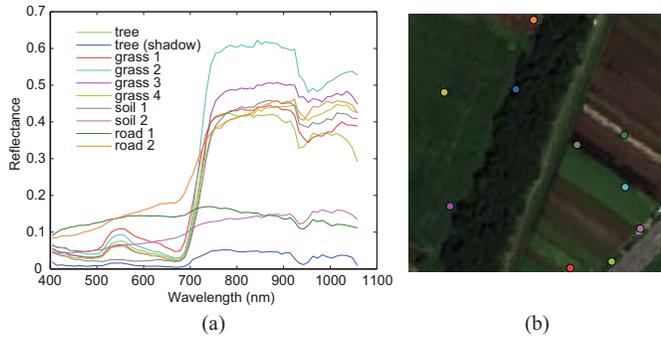

Fig. 3.   (a) Endmember spectra and (b) location of endmembers.

contain errors. Hereafter, we refer to the NMF and semi-NMF method as semi-NMF. To avoid overfitting, early stoppage is adopted in the optimization by setting the number of iterations to 300.

Secondly, semi-NMF is compared with the conventional methods, i.e., FCLS and GDA, which are based on the LMM and GBM, respectively. To evaluate the robustness for spectral complexity and the collinearity issue, we use two types of synthetic dataset generated with different numbers of endmembers. Tables I and II show the results of unmixing performance for the synthetic datasets with three and four endmembers, respectively. FCLS shows the smallest RMSE of abundance fractions for image 1 in the first scenario. In Tables I and II, semi-NMF shows the smallest REs of unmixing for all the images in both scenarios and the smallest RMSEs of abundance fractions for images 2 and 3 in the first scenario. This indicates that the semi-NMF method can converge to a good local optimum with accurate endmember spectra. When endmember spectra contain errors in the second scenario, the RMSE of abundance fractions markedly increases for all the images, and even the REs of unmixing are comparable with those in the first scenario. For both combinations of endmembers (Tables I and II), the difference in RMSE between the first and second scenarios is much larger than the difference in RMSE between the linear and bilinear spectral unmixing methods. This suggests that the accuracy of endmember spectra has a larger effect on the final abundance estimation than the second-order scattering effect. When the number of endmembers increases, as shown in Table II, in the first scenario, the REMS of abundance fractions increases for

TABLE I
COMPARISON OF UNMIXING PERFORMANCES WITH THREE ENDMEMBERS (VEGETATION, SOIL, AND WATER) USING ACTUAL AND ESTIMATED ENDMEMBERS (FIRST AND SECOND SCENARIO): REs AND SAMs OF UNMIXING AND RMSEs OF ABUNDANCE FRACTIONS

	First Scenario					
	RE ($\times 10^{-2}$)			RMSE ($\times 10^{-2}$)		
	FCLS	GDA	Semi-NMF	FCLS	GDA	Semi-NMF
Image 1	1.212	1.212	**1.210**	**0.409**	0.410	0.416
Image 2	1.280	1.255	**1.216**	2.425	2.356	**2.169**
Image 3	1.253	1.236	**1.216**	1.691	1.650	**1.519**
	Second Scenario					
	RE ($\times 10^{-2}$)			RMSE ($\times 10^{-2}$)		
	FCLS	GDA	Semi-NMF	FCLS	GDA	Semi-NMF
Image 1	1.417	1.305	**1.293**	7.480	**7.201**	7.348
Image 2	1.426	1.378	**1.374**	8.448	**8.388**	8.435
Image 3	1.465	1.314	**1.298**	7.739	7.440	**7.408**

TABLE II
COMPARISON OF UNMIXING PERFORMANCES WITH FOUR ENDMEMBERS (TWO VEGETATION, SOIL, AND WATER) USING ACTUAL AND ESTIMATED ENDMEMBERS (FIRST AND SECOND SCENARIO): REs AND SAMs OF UNMIXING AND RMSEs OF ABUNDANCE FRACTIONS

	First Scenario					
	RE ($\times 10^{-2}$)			RMSE ($\times 10^{-2}$)		
	FCLS	GDA	Semi-NMF	FCLS	GDA	Semi-NMF
Image 1	1.449	1.449	**1.447**	**1.985**	**1.985**	2.002
Image 2	1.483	1.494	**1.450**	6.053	5.902	**5.390**
Image 3	1.466	1.471	**1.452**	4.449	4.342	**4.035**
	Second Scenario					
	RE ($\times 10^{-2}$)			RMSE ($\times 10^{-2}$)		
	FCLS	GDA	Semi-NMF	FCLS	GDA	Semi-NMF
Image 1	1.544	1.569	**1.480**	7.325	7.285	**7.258**
Image 2	1.499	1.520	**1.427**	7.627	7.487	**7.484**
Image 3	1.549	1.571	**1.429**	8.385	8.187	**8.151**

all the methods, which may be due to the collinearity issue caused by the highly correlated spectra between endmembers and interacting virtual endmembers. Even in this case, with accurate endmember spectra, GDA and semi-NMF outperform FCLS for images 2 and 3. This confirms that GBM-based unmixing has potential for dealing with spectral complexity. According to the smallest RMSEs of abundance fractions, semi-NMF is a promising optimization method for GBM-based nonlinear unmixing.

IV. EXPERIMENT FOR REAL DATA

GBM-based unmixing using semi-NMF is applied to airborne hyperspectral data to evaluate the numerical unmixing performance for real data, to examine the impact of endmember extraction on bilinear spectral unmixing, and to demonstrate the difference in the abundance map obtained between the LMM and GBM. The dataset was acquired using the compact airborne spectrographic imager (CASI-3) on June 19, 2009. The study area was the agricultural field in the Motonopporo farm in Hokkaido, Japan, because multiple

TABLE III
COMPARISON OF REs ($\times 10^{-3}$) AND SAMs (IN DEGREE), AND COMPUTATIONAL COSTS (INs)

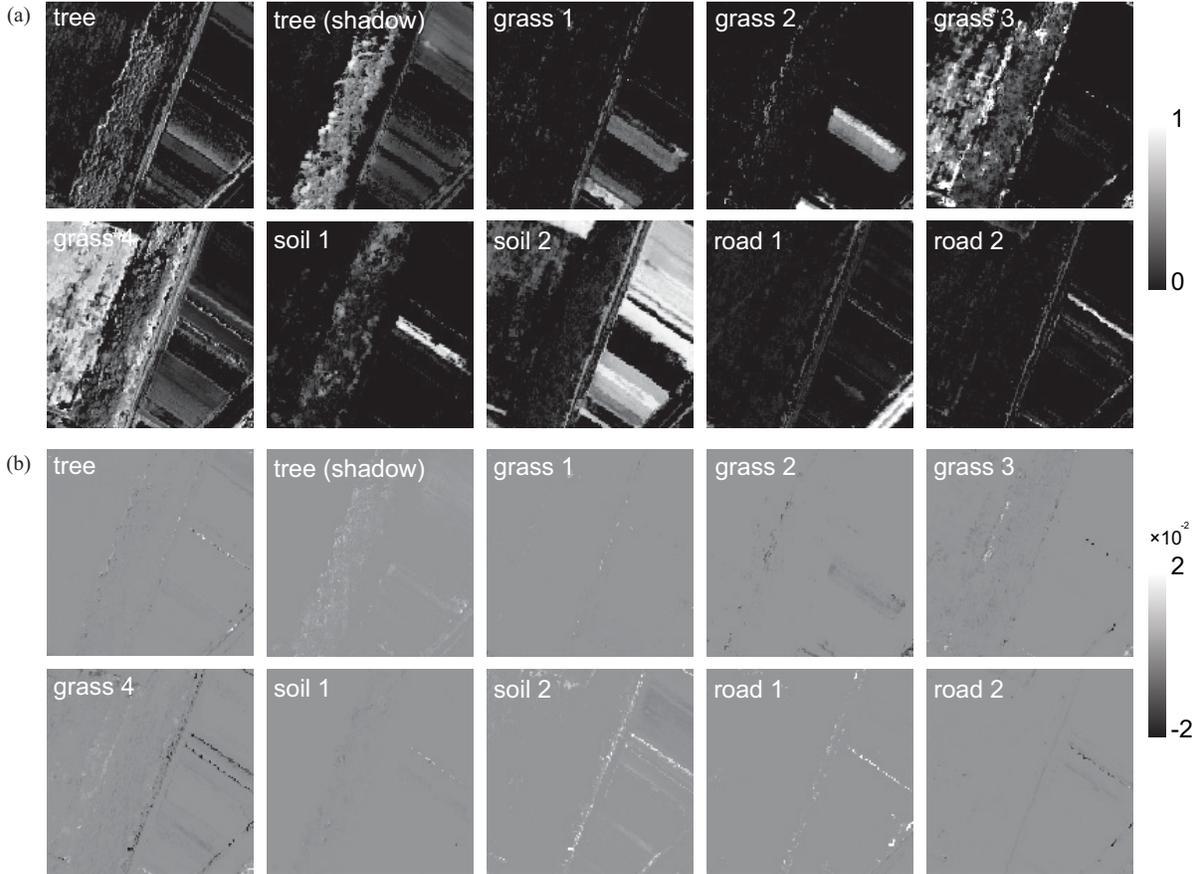|	$D = 6$			$D = 11$			$D = 16$			$D = 21$		
	RE	SAM	Time	RE	SAM	Time	RE	SAM	Time	RE	SAM	Time
FCLS	10.56	2.695	**20.5**	6.320	1.824	**57.4**	5.025	1.488	**95.2**	4.738	1.433	**143.5**
GDA	10.55	2.692	122.2	6.318	1.823	223.1	5.048	**1.479**	670.6	4.721	1.431	785.7
Semi-NMF	**10.26**	**2.640**	55.4	**6.258**	**1.816**	106.6	**4.975**	1.483	169.7	**4.701**	**1.429**	250.4

Fig. 4. (a) Abundance maps and (b) differences of abundance maps with LMM.

scattering is a common phenomenon between vegetation and soil [1]–[5]. The area consisted of a devastated grassland, trees, unpaved rural roads, an agricultural field, and an asphalt road. We selected a 150×150-pixel-size image with 68 spectral channels over 410–1070 nm and a 1-m ground sampling distance. The data initially measured as radiance was converted into reflectance.

The performance of the proposed method is numerically evaluated by the RE and the spectral angle mapper (SAM) of unmixing, and the computational time of Matlab implementations was compared with that of FCLS and GDA. The CPU used is Intel Core i7 CPU 2.80 GHz, with a memory capacity of 16 GB. SAM is calculated using the observed ($\mathbf{y}_l$) and estimated ($\widehat{\mathbf{y}}_l$) spectra as

$$\text{SAM} = \frac{1}{P} \sum_{l=1}^{P} \arccos \left(\frac{\mathbf{y}_l \cdot \widehat{\mathbf{y}}_l}{\|\mathbf{y}_l\| \, \|\widehat{\mathbf{y}}_l\|} \right). \quad (18)$$

RE and SAM are common criteria for evaluating the performance of the unmixing procedure for real datasets. By changing the number of endmembers extracted by VCA and comparing the second-order interaction term and the residual errors of the GBM, we examined the impact of endmember extraction on bilinear unmixing. The effects of the interaction term and the residual errors of unmixing at a single pixel are calculated by the root-sum-square (RSS) method. After the endmember extraction, abundance maps and the impact of bilinear spectral mixing on these abundance maps are calculated.

Table III shows a comparison of the RE and SAM values, and the computational cost determined using four different numbers of endmembers, i.e., $D = 6, 11, 16$, and 21. The Semi-NMF method shows the best performance in terms of RE and SAM for many different numbers of endmembers. In addition, the computational time is smaller than for GDA. In particular, even when the number of endmembers increases,

the semi-NMF method converges to good local optima at reasonable computational cost owing to the simple update rules in matrix form. This result indicates that semi-NMF is a practical method of solving the optimization of GBM-based unmixing owing to its convergence performance and simple implementation.

Fig. 2 shows RSS maps of the second-order interaction term and unmixing residual errors. As the number of endmembers increases (6, 11, 16, and 21), the two maps converge. We concluded that 16 endmembers are sufficient. In spite of the large number of endmembers, the bilinear spectral mixing effect clearly appears in areas B and C in Fig. 2, i.e., the boundary between grass and trees, and the narrow path, where there is a 3-D multilayered structure, which is consistent with the physical model of GBM-based unmixing. With $D = 6$, area A in Fig. 2, corresponding to grass, shows a large bilinear spectral mixing effect; however, the residual error still remains large in this area. It significantly decreases after grass is detected as the endmember at $D = 11$. This means that endmember extraction has a larger influence on residual errors of unmixing than the bilinear mixing effect, which is also confirmed from the difference between the first and second scenarios in the simulation of synthetic datasets. Therefore, to discuss nonlinear spectral mixing, accurate endmember extraction is necessary.

Since VCA is sensitive to the outlier, it can detect some endmembers that are only present in very specific regions. To visualize the abundance map and the bilinear mixing effect, we manually eliminated such type of specific endmembers and reprocessed GBM-based unmixing with 10 endmembers, as shown in Fig. 3(a). In Fig. 3(b), the colored circles indicate the locations of these endmembers, with each color corresponding to that of the spectrum in Fig. 3(a). The endmembers are labeled by visual judgment considering the locations of endmembers and comparing the abundance maps and RGB color image. Fig. 4(a) and (b) show the abundance maps for these 10 materials and their differences from the LMM, which demonstrate the impacts of the second-order interaction on abundance maps. In some regions, the abundance fractions changed by more than 2% compared to the LMM because of the multiple scattering effects. Grass 4 and soil 2 show relatively large changes from the LMM at their boundary owing to the second-order scattering interaction, which is consistent with previous research reports on multiple interactions that often occur between vegetation and soil. This qualitative result implies that GBM-based unmixing using semi-NMF has potential for dealing with the spectrally complex BMM in hyperspectral unmixing.

V. Conclusion

In this paper, we presented a novel optimization method based on semi-NMF for GBM-based nonlinear unmixing. Semi-NMF enables the optimization of GBM-based unmixing to process a whole image in matrix form with simple update rules. The performance of the proposed method is evaluated using synthetic hyperspectral datasets, considering the robustness for the error of endmember extraction and the collinearity

issue, and compared with the LMM-based method and the conventional optimization for GBM-based unmixing. With accurate endmember spectra, GBM-based unmixing showed robust results for the spectral complexity and collinearity issue. In particular, the semi-NMF method gave the smallest RMSE of abundance fractions. The errors of endmember extraction resulted in RMSEs of abundance fractions being larger than the difference in RMSE between the LMM and the GBM. Therefore, accurate endmember extraction is necessary to discuss nonlinear unmixing. We applied GBM-based unmixing using semi-NMF to a real airborne hyperspectral image taken over an agricultural field with many endmembers. The semi-NMF method could be used to visualize the interaction between vegetation and soil and its effect on final abundance maps at reasonable computational cost.

References

[1] D. A. Roberts, M. O. Smith, and J. B. Adams, "Green vegetation, nonphotosynthetic vegetation, and soils in AVIRIS data, " *Remote Sens. Environ.*, vol. 44, nos. 2–3, pp. 117–126, May 1993.

[2] C. C. Borel and S. A. W. Gerstl, "Nonlinear spectral mixing models for vegetative and soil surfaces," *Remote Sens. Environ.*, vol. 47, no. 3, pp. 403–416, Mar. 1994.

[3] T. W. Ray and B. C. Murray, "Nonlinear spectral mixing in desert vegetation," *Remote Sens. Environ.*, vol. 55, no. 1, pp. 59–64, Jan. 1996.

[4] L. Zhang, D. Li, Q. Tong, and L. Zheng, "Study of the spectral mixture model of soil and vegetation in PoYang Lake area, China," *Int. J. Remote Sens.*, vol. 19, no. 11, pp. 2077–2084, 1998.

[5] B. Somers, K. Cools, S. Delalieux, J. Stuckens, D. V. Der Zande, W. W. Verstraeten, and P. Coppin, "Nonlinear hyperspectral mixture analysis for tree cover estimates in orchards," *Remote Sens. Environ.*, vol. 113, no. 6, pp. 1183–1193, Jun. 2009.

[6] J. F. Mustard, L. Li, and G. He, "Compositional gradients across mare-highland contacts: The importance and geological implications of lateral mixing," *J. Geophys. Res.—Planets*, vol. 103, pp. 419–425, Aug. 1998.

[7] R. Close, P. Gader, A. Zare, J. Wilson, and D. Dranishnikov, "Endmember extraction using the physics-based multi-mixture pixel model," *Proc. SPIE*, vol. 8515, p. 85150L, Aug. 2012.

[8] R. Close, "Endmember and proportion estimation using physics-based macroscopic and microscopic mixture models," Ph.D. dissertation, Dept. Comput. Eng., Florida Univ., Gainesville, FL, USA, Dec. 2011.

[9] W. Fan, B. Hu, J. Miller, and M. Li, "Comparative study between a new nonlinear model and common linear model for analysing laboratory simulated-forest hyperspectral data," *Int. J. Remote Sens.*, vol. 30, no. 11, pp. 2951–2962, Jun. 2009.

[10] J. M. Nascimento and J. M. Bioucas-Dias, "Nonlinear mixture model for hyperspectral unmixing," *Proc. SPIE*, vol. 7477, p. 74770I, Sep. 2009.

[11] A. Halimi, Y. Altmann, N. Dobigeon, and J. Tourneret, "Nonlinear unmixing of hyperspectral images using a generalized bilinear model," *IEEE Trans. Geosci. Remote Sens.*, vol. 49, no. 11, pp. 4153–4162, Nov. 2011.

[12] A. Halimi, Y. Altmann, N. Dobigeon, and J. Tourneret, "Unmixing hyperspectral images using the generalized bilinear model," in *Proc. IEEE Int. Geosci. Remote Sens. Symp.*, Jul. 2011, pp. 1886–1889.

[13] J. M. Bioucas-Dias, A. Plaza, N. Dobigeon, M. Parente, Q. Du, P. Gader, and J. Chanussot, "Hyperspectral unmixing overview: Geometrical, statistical, and sparse regression-based approaches," *IEEE J. Sel. Topics Appl. Earth Observ. Remote Sens.*, vol. 5, no. 2, pp. 354–379, Apr. 2012.

[14] B. Hapke, *Theory of Reflectance and Emittance Spectroscopy*. Cambridge, U.K.: Cambridge Univ. Press, 1993.

[15] S. Weisberg, *Applied Linear Regression*. New York, NY, USA: Wiley, 1985.

[16] X. Chen, J. Chen, X. Jia, B. Somers, J. Wu, and P. Coppin, "A quantitative analysis of virtual endmembers' increased impact on the collinearity effect in spectral unmixing," *IEEE Trans. Geosci. Remote Sens.*, vol. 49, no. 8, pp. 2945–2956, Aug. 2011.

[17] D. D. Lee and H. S. Seung, "Learning the parts of objects by nonnegative matrix factorization," *Nature*, vol. 401, pp. 788–791, Oct. 1999.

[18] D. D. Lee and H. S. Seung, "Algorithms for non-negative matrix factorization," in *Proc. Conf. Adv. Neural Inf. Process. Syst.*, vol. 13, 2001, pp. 556–562.

[19] L. Miao and H. Qi, "Endmember extraction from highly mixed data using minimum volume constrained nonnegative matrix factorization," *IEEE Trans. Geosci. Remote Sens.*, vol. 45, no. 3, pp. 765–777, Mar. 2007.

[20] S. Jia and Y. Qian, "Constrained nonnegative matrix factorization for hyperspectral unmixing," *IEEE Trans. Geosci. Remote Sens.*, vol. 47, no. 1, pp. 161–173, Jan. 2009.

[21] A. Huck, M. Guillaume, and J. Blanc-Talon, "Minimum dispersion constrained nonnegative matrix factorization to unmix hyperspectral data," *IEEE Trans. Geosci. Remote Sens.*, vol. 48, no. 6, pp. 2590–2602, Jun. 2010.

[22] X. Liu, W. Xia, B. Wang, and L. Zhang, "An approach based on constrained nonnegative matrix factorization to unmix hyperspectral data," *IEEE Trans. Geosci. Remote Sens.*, vol. 49, no. 2, pp. 757–772, Feb. 2011.

[23] C. Ding, T. Li, and M. I. Jordan, "Convex and semi-nonnegative matrix factorization," *IEEE Trans. Patten Anal. Mach. Intell.*, vol. 32, no. 1, pp. 45–55, Jan. 2010.

[24] D. C. Heinz and C.-I. Chang, "Fully constrained least squares linear spectral mixture analysis method for material quantification in hyperspectral imagery," *IEEE Trans. Geosci. Remote Sens.*, vol. 39, no. 3, pp. 529–545, Mar. 2001.

[25] J. M. Nascimento and J. M. Bioucas-Dias, "Vertex component analysis: A fast algorithm to unmix hyperspectral data," *IEEE Trans. Geosci. Remote Sens.*, vol. 43, no. 4, pp. 898–910, Apr. 2005.

Jocelyn Chanussot (M'04–SM'04–F'12) received the M.Sc. degree in electrical engineering from the Grenoble Institute of Technology (Grenoble INP), Grenoble, France, and the Ph.D. degree from Savoie University, Annecy, France, in 1995 and 1998, respectively.

He was with the Geography Imagery Perception Laboratory, Delegation Generale de l'Armement (DGA - French National Defense Department), Bagneux, France, in 1999. Since 1999, he has been with Grenoble INP, where he was an Assistant Professor from 1999 to 2005, an Associate Professor from 2005 to 2007, and is currently a Professor of signal and image processing. He is currently conducting his research at the Grenoble Images Speech Signals and Automatics Laboratory (GIPSA-Lab). His current research interests include image analysis, multi-component image processing, nonlinear filtering, and data fusion in remote sensing.

Dr. Chanussot is the founding President of IEEE Geoscience and Remote Sensing French chapter (2007–2010) which received the 2010 IEEE GRS-S Chapter Excellence Award "for excellence as a Geoscience and Remote Sensing Society chapter demonstrated by exemplary activities during 2009." He was the recipient of the NORSIG 2006 Best Student Paper Award, the IEEE GRSS 2011 Symposium Best Paper Award and of the IEEE GRSS 2012 Transactions Prize Paper Award. He was a member of the IEEE Geoscience and Remote Sensing Society AdCom (2009–2010), in charge of membership development. He was the General Chair of the first IEEE GRSS Workshop on Hyperspectral Image and Signal Processing, Evolution in Remote sensing (WHISPERS). He is the Chair (2009–2011) and was the Cochair of the GRS Data Fusion Technical Committee (2005–2008). He was a member of the Machine Learning for Signal Processing Technical Committee of the IEEE Signal Processing Society (2006–2008) and the Program Chair of the IEEE International Workshop on Machine Learning for Signal Processing, (2009). He is an Associate Editor for the IEEE GEOSCIENCE AND REMOTE SENSING LETTERS (2005–2007) and for *Pattern Recognition* (2006–2008). Since 2007, he has been an Associate Editor for the IEEE TRANSACTIONS ON GEOSCIENCE AND REMOTE SENSING. Since 2011, he has been the Editor-in-Chief of the IEEE JOURNAL OF SELECTED TOPICS IN APPLIED EARTH OBSERVATIONS AND REMOTE SENSING.

Naoto Yokoya (S'10) received the M.Sc. and Ph.D. degrees in aerospace engineering from the University of Tokyo, Tokyo, Japan, in 2010 and 2013, respectively.

He has been a Research Fellow with the Japan Society for the Promotion of Science, since 2012. His current research interests include hyperspectral data analysis.

Akira Iwasaki received the M.Sc. degree in aerospace engineering and the Doctoral degree in engineering from the University of Tokyo, Tokyo, Japan, in 1987 and 1996, respectively.

He joined the Electrotechnical Laboratory, where he engaged in research on space technology and remote sensing system in 1987. He is currently a Professor with the University of Tokyo.